Spatial distribution of volcanoes on Io: implications for tidal heating and magma ascent

Christopher W. Hamilton[1], Ciarán D. Beggan[2], Susanne Still[3], Mikael Beuthe[4], Rosaly M. C. Lopes[5], David A. Williams[6], Jani Radebaugh[7], and William Wright[3]

[1]Planetary Geodynamics Laboratory, NASA Goddard Space Flight Center, Greenbelt, MD, USA, [2]British Geological Survey, Edinburgh, UK, [3] Information and Computer Sciences, University of Hawai'i at Mānoa, Honolulu, USA, [4]Royal Observatory of Belgium, Brussels, Belgium, [5]Jet Propulsion Laboratory, California Institute of Technology, Pasadena, USA, [6]School of Earth and Space Exploration, Arizona State University, Tempe, USA, [7]Geological Sciences, Brigham Young University, Provo, USA.

Contact information for the corresponding author (Christopher W. Hamilton):

Mailing address: Planetary Geodynamics Laboratory, NASA Goddard Space Flight Center, Mail Code 698, Greenbelt, MD, USA 20771, USA

e-mail: christopher.hamilton@nasa.gov

Phone number: (office) 301.614.6749, (mobile) 301.305.3818

Keywords

Io; volcanism; hotspots; paterae; spatial distribution; tidal dissipation; interior; heating

Abstract

Extreme volcanism on Io results from tidal heating, but its tidal dissipation mechanisms and magma ascent processes are poorly constrained. Here we analyze the distribution of volcanic hotspots and paterae identified within the first 1:15,000,000-scale global geologic map of Io to characterize their patterns of spatial organization. Ionian hotspots correspond to the locations of observed positive thermal anomalies, whereas paterae are caldera-like volcano-tectonic depressions that record locations of volcanic activity over a longer period of geologic time. Some (~20%) of patera floor units are associated with active hotspots, but the majority appear to be extinct or dormant at the time of observation. Volcano distributions are useful for testing interior models of Io because the relative strength of tidal heating in the asthenosphere and deep-mantle greatly affect expected patterns of surface heat flux. We examine the distribution of volcanic centers using nearest neighbor (NN) statistics and distance-based clustering. Nearest neighbor analysis reveals hotspots to be globally random, but closer to the equator, they are uniform (i.e., more widely spaced than a random model would predict). This implies that magma scavenging and/or tectonic controls around active volcanic systems in near-equatorial region may drive hotspots apart. Globally, vigorous mantle convection and/or deep-mantle heating may reduce surface heat flux variations and promote randomness within the overall hotspot distribution. In contrast to the hotspots, NN patera floor units are globally clustered, but randomly distributed near the equator. This implies that on a global-scale patera floor units tend to concentrate close to one another, but in the most densely populated near-equatorial region, overprinting may randomize their distribution over time. Distance-based clustering results support a dominant role for asthenospheric heating within Io, but show a 30–60° eastward offset in volcano concentrations from predicted locations of maximum surface heat flux along the tidal axis. This

offset may imply faster than synchronous rotation, a role for lateral advection of magma within Io's interior prior to its eruption, state of stress controls on the locations of magma ascent, and/or a missing component in existing tidal dissipation models, such as the effects of fluid tides generated within a globally extensive magma ocean.

1. Introduction

Io, the innermost of Jupiter's Galilean satellites, is the most volcanically active body in the Solar System. Io's global mean heat flow is not precisely known, but estimates generally range from 1.5–4 W m^{-2} (Moore et al., 2007), with the most recent astrometric observations supporting a value of 2.24 ± 0.45 W m^{-2} (Lainey et al., 2009). This mean surface heat flux is ~20 times larger than the Earth's (Turcotte and Schubert, 2002), but unlike the Earth, Io's internal heat comes primarily from the dissipation of tidal energy and not from radiogenic sources (Peale et al., 1979; Moore et al., 2007). Io's Laplace resonance with Europa and Ganymede maintains all three satellites in noncircular orbits, which results in continuous deformation and frictional heating of the satellite's interior (e.g., Peale et al., 1979; Ross and Schubert, 1985; Ross et al., 1990; Schubert et al., 1986; Segatz et al., 1988; Tackley, 2001; Tackley et al., 2001; Moore et al., 2007). Heat produced within Io's interior is dominantly advected to the surface by ascending silicate magma and not conducted through its lithosphere (McEwen et al., 2004). The heat-pipe mechanism proposed for transporting Io's internal thermal energy to the surface (O'Reilly and Davies, 1981) involves bringing magma upward through "hotspots" that are embedded within a relatively cold lithosphere. Analysis of Io's global distribution of volcanoes (Fig. 1) can therefore provide information about the moon's internal structure, thermo-rheological properties, tidal dissipation mechanisms, processes of melt generation, and magma transport. Better understanding these processes for Io may also provide insights into similar tidal heating mechanisms operating on other worlds, such as Europa and Enceladus, as well as some tidally-heated exoplanets.

2. Io’s internal structure and its relation to tidal dissipation models

The *Galileo* mission revealed that Io is a differentiated body consisting of a metallic iron core, with a radius of 650–950 km, surrounded by a silicate mantle (Moore et al., 2007). The thickness and composition of the crust are unknown, but must contribute to a strong lithosphere that is capable of supporting the elastic stresses that are associated with mountains up to ~18 km in height (Schenk et al., 2001; Jaeger et al., 2003). The structure and temperature distribution within the mantle are debated, but Keszthelyi et al. (2007) suggest a potential temperature between 1523 and 1723 K, with a preferred value of ∼1573 K. They also claim that the top of the mantle is likely partially molten, with 20–30 vol. % rock melt. The presence of a global layer with ≥20% interconnected partial melt and >50 km thickness (i.e., the proposed asthenosphere) is consistent with *Galileo* magnetometer data of Io’s induced magnetic field (Khurana et al., 2011).

In end-member tidal dissipation models, the bulk of Io’s heating occurs either within the deep-mantle or within the asthenosphere (Ross and Schubert, 1985; Schubert et al., 1986; Segatz et al., 1988; Tackley et al., 2001), while in mixed models heating is partitioned between these end-members (Ross et al., 1990; Tackley et al., 2001). Computations of heat production usually assume a spherically symmetric interior (for a 3D approach see Běhounková et al., 2010) having a linear viscoelastic rheology of the Maxwell type. In the simplest approximation, heat is transferred radially to the surface by an unspecified mechanism, but in more realistic models, heat is transported either by convective flow (Tackley et al., 2001) or by melt segregation

(Moore, 2001). In deep-mantle heating models (Fig. 2a), the surface heat flux is maximum near the poles and minimum at the equator, with absolute minima occurring at the subjovian (0°N, 0°W) and antijovian points (0°N, 180°W). In asthenospheric models, heat flux is minimum at the poles and maximum in the equatorial area, with primary maxima occurring north and south of the subjovian and antijovian points (at approximately ±30° latitude), and with secondary maxima occurring at the centers of the leading (0°N, 90°W) and trailing (0°N, 270°W) hemispheres (Fig. 2b). Spatial variations in surface heat flux are lower in mixed models, with maxima progressively migrating towards the poles as deep-mantle heating is added to the asthenospheric heating component (Figs. 2c, 2d). Moderate convection does not fundamentally change these patterns, but as convection becomes more vigorous (i.e., for increasingly large Rayleigh numbers), horizontal flows will smooth out lateral heat flux variations. The amplitude of surface heat variations reduces in inverse proportion to their wavelength (Tackley, 2001), and ultimately erases them if the Rayleigh number becomes very large. The deep-mantle heating pattern is nearly pure harmonic degree-2 and therefore convection uniformly reduces the amplitude of surface heat flux variations. By contrast, the strong degree-4 harmonic component in the asthenospheric pattern is reduced more greatly by lateral flows than the degree-2 component, and so the resulting structure shows more heat concentration near the equator, particularly close to the subjovian and antijovian points (Fig. 2e).

Surface heat flux patterns in Figure 2 are computed with spherically symmetric interior models having three or four homogeneous incompressible layers (Segatz et al., 1988; Spohn, 1997). All models have a fluid core, a viscoelastic mantle with a Maxwell rheology and a thin elastic lithosphere or crust. In asthenospheric models, the mantle is subdivided into a high-viscosity deep mantle and a low-viscosity asthenosphere. The core radius, core density, mantle density, and lithospheric thickness are chosen to be 980 km, 5150 kg/m^3, 3200 kg/m^3 and 30 km, respectively, as in Segatz et al. (1988). These parameters represent only one example of a possible interior structure of Io (see Moore et al., 2007, and Turtle et al., 2007, for alternative examples), but these choices are not crucial for the computation of dissipation patterns. The most important factor is the rheology of the mantle and specifically the presence (or absence) of an asthenosphere. The thickness of the asthenosphere (if indeed present) is set to 50 km, which is the lower bound for the global magma layer discussed in Khurana et al. (2011). We solve the equations for displacement, stress, and gravitational perturbation with the propagator matrix technique (e.g., Sabadini and Vermeersen, 2004; Roberts and Nimmo, 2008) and compute the dissipation rate per unit volume by summing on the squared strains (Peale and Cassen, 1978; Segatz et al., 1988; Tobie et al., 2005). The surface heat flux is computed with the assumption that the heat flows radially to the surface. The unknown shear modulus μ and viscosity η of the lithosphere are set to $\mu = 65 \times 10^9$ Pa and $\eta = 10^{23}$ Pa·s, and for the deep-mantle they are $\mu = 60 \times 10^9$ Pa and $\eta = 10^{20}$ Pa·s, as in Segatz et al. (1988). The shear modulus and viscosity of the upper-mantle and asthenosphere are chosen in order to generate the correct total power of about 10^{14} W (Moore et al., 2007). In the deep-mantle end-member heating model (Fig. 2a), the upper-mantle has $\mu = 3.5 \times 10^9$ Pa and $\eta = 10^{15}$ Pa·s. In the asthenospheric end-member model (Fig. 2b), the asthenosphere has $\mu = 4 \times 10^4$ Pa and $\eta = 10^{10}$ Pa·s. Figure 2c shows a mixed model with a linear combination of 1/3 deep-mantle and 2/3 asthenospheric heating. The minimum surface heat flux variance model (Fig. 2d) was generated by a mixture of 61% deep-mantle ($\mu = 3.5 \times 10^9$ Pa, $\eta = 4.7 \times 10^{14}$ Pa·s) and 39% asthenospheric ($\mu = 3 \times 10^4$ Pa, $\eta = 10^{10}$ Pa·s) heating. The effect of lateral flows on the asthenospheric pattern (Fig. 2e) is approximated with the scaling law for boundary-focused heating (Eq. 11 of Tackley, 2001). For our asthenospheric model, the

Rayleigh number for internal heating is 7.2×10^{13} (see Eq. 5 of Tackley, 2001), with the heat capacity, thermal diffusivity and thermal expansivity as in Table 1 of Tackley (2001). The non-zero harmonic components of the heat flux are reduced by factors of 9.6 (degree-2, aspect ratio 60) and 19.2 (degree-4, aspect ratio 30).

If the assumption that volcanic centers are directly correlated with surface heat flux is correct, then the spatial distribution of volcanoes Io may be used to distinguish between these tidal dissipation models. Previous studies (e.g., Carr et al., 1998; McEwen et al., 1998; Lopes-Gautier et al., 1999), suggested that the global distribution of volcanic centers on Io appears "uniform", by which they mean homogenously distributed over the moon's surface, but not necessarily spaced at regular intervals. However, they also noted higher concentrations of volcanoes at low latitudes. This result is consistent with tidal dissipation occurring mostly in the asthenosphere than the deep-mantle (Lopes-Gautier et al., 1999). Others have shown that volcanic centers (some of which are active hotspots) are clustered within several tens of degrees of the subjovian or antijovian points (e.g., Radebaugh et al., 2001; Schenk et al., 2001; Tackley et al., 2001; Veeder et al., 2011). Kirchoff et al. (2011) also identified a dominant degree-2 clustering pattern among volcanic centers using spherical harmonic analysis, but they note that the higher degrees of the power spectrum are consistent with randomness and even repelling (i.e., greater than random spacing). To explore the statistical significance of these contrasting observations, we reexamine the spatial distribution of hotspots and paterae on Io at multiple scales using several statistical techniques and insights from new global geologic maps (Williams et al., 2011a, 2011b).

3. Inventory of hotspots and paterae on Io

Volcanic centers on Io include hotspots and paterae that have been identified using spacecraft images and Earth-based telescopes. Ionian hotspots are positive thermal anomalies associated with sites of active volcanism, whereas paterae are caldera-like volcanic-tectonic depressions (described below) that may, or may not, be currently active. Approximately two-thirds of the 173 hotspots are located within patera floor units (Williams et al., 2011), which implies ~20% of the patera floor units ($N = 529$) were volcanically active at the time of observation. Additional paterae may be also active, but their thermal anomalies have not been resolved to date given temporal, spatial, and other thermal remote sensing constraints. Hotspots located outside patera structures may either represent primary volcanic systems lacking a well-developed caldera-like feature, or be associated lava flows that have transported hot material away from their source through thermally insulated internal pathways (e.g., lava tubes). Hotspot observations therefore provide a statistical sample of the locations where active volcanic processes have occurred on Io since their initial discovery in 1979 (Smith et al., 1979a, 1979b). In contrast, paterae represent a longer window into Io's volcanic history, spanning ~1 million years (i.e., Io's timescale of resurfacing; McEwen et al., 2000a; McEwen et al., 2004). The hotspot database used in this study (Fig. 1a) comprises all thermal anomalies identified in Table A.1 of (Lopes and Spencer, 2007), plus the "East Girru" hotspot (22°N, 235°W) identified by *New Horizons* (Spencer et al., 2007). The database also includes Ra Patera (8.3°S, 325.2°W). Ra Patera lacks an observed positive thermal anomaly, but it is included in our database as hotspot because its activity was confirmed by the detection of an associated volcanic plume (Lopes et al., 2004).

Paterae on Io are generally interpreted to be morphologically analogous to terrestrial calderas (Carr et al. 1998; Radebaugh et al., 2001; McEwen et al., 2004). Paterae have a wide range of shapes, ranging from circular to irregular, with irregular paterae thought to have formed under the influence of structural or tectonic controls (see Radebaugh et al., 2001 for a complete overview). Patera floors show a wide range of complexity, depending upon the spatial resolution of the images. At high resolution, patera floor units contain a mixture of relatively bright and dark features, irregular hummocks, and pits (e.g., Chaac Patera; Williams et al., 2002). At lower resolution, patera floors range from dark gray to black to bright pinkish-white to red-orange in color, with considerable variation in monochromatic albedo, color, and texture (Williams et al., 2011). Dark patera floor units often correlate with *Galileo* Near Infrared Mapping Spectrometer (NIMS) and Photopolarimeter-Radiometer (PPR) hotspots. Bright patera floor units tend not correlate with hotspots and NIMS data indicate an enhanced signature of sulfur dioxide in the white to pinkish-white material on several patera floors. These observations suggest that bright patera floor units exhibit colder temperatures and are inactive (Lopes et al., 2004). Based on morphological and mapping studies, Io's patera floor units are interpreted to be composed of lava flows, lava ponds, or lava lakes, in which darker units are thought to be silicate in composition, whereas brighter flows are either sulfur-rich materials or cold silicates covered by a mantle of sulfur-rich plume deposits ±SO_2 frosts (Keszthelyi et al., 2001; Radebaugh et al., 2001; Turtle et al, 2004; Williams et al., 2002, 2004, 2005, 2007, 2011).

In the first complete 1:15,000,000-scale global geologic map of Io (Williams et al., 2011a, 2011b), patera floor units were mapped as bright, dark, and undivided, with some paterae being completely filled by a single floor unit, while others exhibit multiple units. The map was produced in ArcGIS using a set of combined *Galileo-Voyager* image mosaics reprocessed to a spatial resolution of 1 km/pixel (Becker and Geissler, 2005). There is some discrepancy between different workers on the number of paterae on Io (e.g., Radebaugh et al., 2001, Veeder et al., 2001; Williams et al., 20111, 2011b), based on the different approaches used to define and identify paterae. In this study, we focus on the 529 patera floor units mapped by Williams et al. (2011a; Fig. 1b), but also consider a modified distribution of 581 patera floor units presented by Williams et al. (2011b; Fig. 1b). In addition, to these databases, we aggregated the 581 patera floor units into 423 generalized patera structures that are intended to represent the locations of volcanic systems (Fig. 1a). These patera locations were obtained in ArcGIS by calculating the centroids of amalgamated patera floor units that are confined within topographic depressions. Coordinates for all hotspots (N =173), patera floor units (N = 529 and 581) and paterae structures (N = 423) are provided as Supplementary Material.

Although global geologic maps of Io (Williams et al., 2011a, 2011b) are based on 1 km/pixel Galile-*Voyager* mosaics, the resolution of the original image data was spatially variable, which raises the possibility of observational bias in the identification of volcanic centers. Figure 1b illustrates the spatial variations in image resolution and suggests that poor quality data poleward of 60°N and 75°S (Fig. 3a) and in the zone from 0° to 90°W (Fig. 3b) may have limited the detection of the smallest paterae in the extreme polar regions and in the subjovian and leading hemispheres. Nonetheless, 83% of Io's surface at better than 5 km/pixel, with only 3% imaged at resolutions less than 10 km/pixel (Fig. 1b), and given that the mean diameter of the patera floor units (N = 529) is 41.6 ±27.6 km (at 1σ), the currently resolved volcanoes distributions are expected to provide a representative sample of the global distribution.

4. Methods

4.1 Nearest neighbor tests for randomness, uniformity, and clustering

To quantitatively characterize the distribution of volcanoes on Io, we developed new geospatial analysis tools to investigate the spatial relationship between points of interest on spherical bodies using nearest neighbor (NN) distance statistics. These tools are incorporated into a MATLAB package called Geologic Image Analysis Software (GIAS Version 2.0), which is freely available from www.geoanalysis.org. Pair-wise distance relationships between nearest NN hotspots and paterae are used to test for statistically significant departures from randomness. Our NN analyses utilize great-circle distances between volcanic centers, accounting for sample-size-dependent calculation biases in NN test statistics (Baloga et al., 2007; Beggan and Hamilton, 2010; Hamilton et al., 2010, 2011). In addition, we consider biases in NN test statistics introduced by analyzing curved regions of interest on the surface of the sphere (first recognized as an issue for NN analyses within this study).

The test statistic *R* is the ratio of the actual mean NN distance $\bar{r}_a$ measured within a point distribution to the expected mean NN distance $\bar{r}_e$ within the region of interest given a model population of equivalent sample-size (Clark and Evans, 1954),

$$R = \frac{\bar{r}_a}{\bar{r}_e} \qquad (1).$$

Based on *R*, a test distribution could be consistent with the expected distribution model, clustered with respect to the model, or more uniform. A second statistic, *c,* evaluates the significance of the result implied by *R* (Clark and Evans, 1954),

$$c = \frac{\bar{r}_a - \bar{r}_e}{\sigma_e} \qquad (2),$$

where σ_e is the expected standard deviation based on a Poisson random distribution with *N* points within an area *A*.

$$\sigma_e = \frac{0.26136}{\sqrt{N^2/A}} \qquad (3).$$

Ideal values of R, c, and their standard deviations vary depending on the number of points N within the distribution and the shape of the region of interest (Fig. 4). Consequently, 1 and 2σ confidence limits are calculated for each test statistic and the significance of R and c are evaluated by taking into account N and the geometry of the region of interest.

The relative value of R and c allow us to make inferences about the nature of the spatial distribution of the points of interest. If R is less than -2σ, $\bar{r}_a$ is clustered relative to the null hypothesis, whereas if R is greater than +2σ, the NN distances tend toward uniformity. If R and c are both outside their respective ±2σ limits, then the input distribution exhibits a statistically significant departure from the null hypothesis, whereas if R and c are both within their ±2σ limits, the null hypothesis cannot be rejected. In this study, the null hypothesis is a homogeneous Poisson model (i.e., spatially random).

Spatial patterns matching the null hypothesis should ideally have $R = 1$ with $c = 0$ (Clark and Evans, 1954). However, Baloga et al., (2007) noticed a significant bias away from the ideal values for R and c in their calculations for low N (<100). Using multiple Monte-Carlo simulations of Poisson random distributions of N points, they computed a sample-size-dependent correction for the expected values of R and c and their standard deviations on a closed flat planar surface. On an approximately spherical body, the biases are different because the surface is open (i.e. there are no boundaries). Hence we compute the correction for R and c using a Monte-Carlo simulation on a sphere rather than a flat plane. To construct random spatial distributions on a unit sphere, we generating N latitude θ and longitude φ pairs using the uniform distribution to compute positions $\theta = \sin^{-1}(2U(N) - 1)$; $\varphi = 2\pi U(N)$, where the uniform random variable $U(N) \in (0,1)$. Angular distances between first NN points approximate a homogeneous Poisson distribution and for Io angular distances are scaled to great-circle distances by multiplying them by the average radius of Io (1,821.46 km). For each region of interest, we perform 4000 Monte Carlo simulations for N ranging from 10 to 1000 to obtain $\bar{r}_e$, ideal values of R and c, and their standard deviations (Fig. 4). Second order exponential curves are fitted through these results for interpolation and plotting purposes. On a full sphere, NN statistics for the expected homogeneous Poisson distributions approach the theoretical values predicted by Clark and Evans (1954), whereas for smaller and increasingly closed areas (e.g., a half, third, and quarter of a sphere) the biases in R and c increase and approach the ideal values for planar (i.e., Euclidean) geometries specified by Baloga et al. (2007).

We analyze volcano centers on Io in following domains: global, northern hemisphere, southern hemisphere, subjovian hemisphere, antijovian hemisphere, leading hemisphere, trailing hemisphere, north polar, south polar, and near-equatorial. Polar and near-equatorial regions are specified by divisions at ±19.47° latitude to divide the surface area of Io into three equal thirds, thereby facilitating comparisons between these NN statistics and minimizing the effects of potential resolution bias by considering large regions. For instance, by dividing the surface area of Io into equal thirds at ±19.47°, the zones of poor quality data poleward of 60°N and 75°S represent less than 20% and 5% of the total surface area in the north and south polar regions, respectively, and so we do not expect observational basis to significantly affect the statistical significance of our NN results.

4.2 Distance-based clustering

Nearest neighbor analyses consider pair-wise distance relationships between objects, but they do not treat how those objects may be organized into larger groups. To identify larger regional groupings among hotspots (N = 173) and patera floor units (N = 529), we use a distance-based clustering technique to partition the volcanic centers into k clusters. For two cluster solutions ($k = 2$), polar clusters would imply deep-mantle heating (Fig. 2a), whereas cluster centers located near the subjovian and antijovian points would imply asthenospheric-dominated tidal dissipation (Fig. 2b). Solutions with six clusters ($k = 6$) are important because asthenospheric-dominated models predict additional structure, with a total of six maxima occurring in surface heat flux distribution (Figs. 2b–e). Limiting our cluster analyses to solutions involving two and six groups is justified by the spherical harmonic analysis of volcanic centers on Io (Kirchoff et al., 2011), which only identified statistically significant clusters (beyond 2σ) at degrees 2 and 6.

The clustering algorithm finds cluster center locations that minimize the total great-circle distance between all points and their nearest cluster center. This is achieved by iteratively assigning points to clusters and re-locating the cluster centers to minimize the objective function. Gradient decent algorithms of this kind (e.g., k-means clustering; Lillesand and Kiefer, 2000) are prone to identifying local minima in the objective function, and so we use an optimization technique known as deterministic annealing (DA; Rose, 1998) to search for the globally optimum cluster center locations.

To perform the distance-based clustering of volcanoes on Io, we construct a maximum entropy model (Shannon, 1948) for each level of information loss (i.e., value of the parameter λ). We then use DA (Rose, 1998) to find the global optimum solution that minimizes the total within cluster great-circle distance $d(\boldsymbol{x}_i, \boldsymbol{x}_j)$ between cluster centers $\boldsymbol{x}_i$ and volcanic centers $\boldsymbol{x}_j$. This is achieved by solving the optimization problem,

$$\min_{p(j|i)\boldsymbol{x}_j,} \sum_{j=1}^{k} \frac{1}{N} \sum_{i=1}^{N} p(j|i) \left(d(\boldsymbol{x}_i, \boldsymbol{x}_j) - \lambda \log_2 \frac{p(j|i)}{p(j)} \right) \qquad (4),$$

subject to $\sum_j p(j|i) = 1$ for all i and $0 \leq p(j|i) \leq 1$, for all j and i, where $\mathbf{x}_j$ and $\mathbf{x}_i$ are vectors containing the latitude and longitude of each point; $j = 1, \ldots, k$; $i = 1, \ldots, N$; N is the number of points within the data set; k is the number of clusters; $p(j)$ is the cluster probability distribution; and $d(\boldsymbol{x}_i, \boldsymbol{x}_j)$ is obtained using the Haversine formula. The DA algorithm computes the optimal partition at each level value of λ by iterating with the following calculation of the cluster membership probability,

$$p(j|i) = \frac{1}{Z(i,\lambda)} e^{-\frac{1}{\lambda} d(x_i, x_j)} \qquad (5),$$

and updating the cluster locations based on the mean of the point locations assigned to them, weighted by $p(j \mid i)$, where $Z = \sum_j e^{\frac{1}{\lambda} d(x,j)}$. The DA algorithm is initialized by specifying k and an annealing rate $\alpha > 1$. The parameter λ is initially set to a large value (i.e., 10^8), which initially associates points to each cluster with equal probability, $p(j \mid i) = 1 / k$. The weight of each cluster $p(j)$ is $1 / k$. The algorithm then enters into two nested loops. The outer loop changes λ by dividing the previous λ by α, while the inner loop computes the cluster membership probabilities $p(j \mid i)$ and updates the locations of each cluster center by iterating Eq. (5) and applying the cluster location update. Optimal $p(j \mid i)$ and optimal cluster center locations for the last value of λ are then used as initial conditions for iterations at the new λ value.

If the annealing rate α is small enough, then the DA algorithm is guaranteed to find the optimal partition of the data, as $\lambda \rightarrow 0$ (Geman and Geman, 1984). Using this method we analyzed the global hotspots and paterae using $k = 2$ and 6, with $\alpha = 1.01$. However, to account for variable power output within (Rathbun et al., 2002) and between (Veeder et al., 2009) volcanic centers, future geospatial analyses may be improved by weighting volcanic centers by their proportion of total power output.

The DA algorithm is guaranteed to find the globally optimum solution, but any meaningful clustering should be stable to sample fluctuations and so we also perform a sensitivity analysis to compare the optimum partitioning of the data to other potentially signifigant solutions. To assess if optimum clustering solutions are significantly better than alternative partitions of the data, we searched for near-optimal solutions by increasing α, over a range from 1.01 to 1010, and repeating the cluster analysis for the hotspot and patera databases until we identified 100,000 unique solutions for the $k = 2$ scenarios and 30,000 solutions for the $k = 6$ scenarios. This search is combinatorial and therefore not exhaustive because that would be computationally prohibitive. Nonetheless, to assess which of these suboptimal solutions are potentially significant, we calculated variance for each of the four clustering problems by randomly perturbing the initial locations of the volcanic centers and performing 1000 repetitions of the DA algorithm. Initial hotspot locations were perturbed by a random distance drawn from a Gaussian distribution with a mean and standard deviation equal to the mean effective radius of all patera floor units ($N = 529$) with uncertainty of 1σ (i.e., 20.8 ±13.8 km). Each patera centroid was perturbed by the effective radius of the corresponding patera floor unit.

In considering which suboptimal solutions are potentially significant, we took a conservative approach and considered all solutions with objective function results (i.e., cumulative distances between all points and their nearest cluster center) within 1σ of the optimum result. For each of these solutions, we calculate the mean displacement of each cluster center from the nearest optimum center. The maximum mean displacement among all of the potentially significant near-optimum solutions provides an estimate of the uncertainty in the cluster analysis (see Supplementary Material for more detail).

5. Results

5.1 Nearest neighbor analyses

The global NN distribution of hotpots on Io is consistent with a homogeneous Poisson model, whereas the global distribution of patera floor units (N = 529) is clustered relative to the null hypothesis (Figs. 5a and 5b). Hotspot NN distances are globally unimodal with a peak at 225–300 km (Fig. 6a), whereas the NN distances between patera floor units are bimodal with a primary mode at distances <75 km and a secondary mode between 150–225 km (Fig. 6a). To explore how sensitive these NN results are to the choice of paterae database, we also examined the patera floor units (N = 581) identified by Williams et al. (2011b) and a database of generalized patera structures (N = 423) that represent volcanic systems.

Analysis of the global distribution of 581 paterae floor units from Williams et al. (2011b) yields identical implications with both the N = 529 and 581 distributions showing statistically significant clustering (beyond 2σ) relative to a homogeneous Poisson model. Specifically, the N = 529 paterae floor distribution has R = 0.89 and c =-4.811, whereas the N = 581 distribution has R = 0.83 and c = -7.82, with both distributions sharing effectively the same sample-size-dependent thresholds of significance (i.e., R = 0.96 and c = -1.98 for the lower 2σ thresholds for statistically significant departures from randomness toward clustering; see Supplementary Material for more detail). The primary difference between these distributions is that the N = 581 distribution has slightly more paterae floor units with NN distances <50 km (Fig. 6b), which accounts for the stronger tendency toward clustering. However, given the similarities between both distributions, we assume that the N = 529 database provides a representative sample and consider only this patera floor unit distribution in our subsequent analyses.

In contrast to the patera floor units, the generalized patera structures exhibit statistically significant departures from the homogeneous Poisson model, with $R = 1.10$ and $c = 4.06$ exceeding their respective upper 2σ thresholds of 1.05 and 2.06 (see Supplementary Material for more detail). This implies that generalized patera are self-organized into a repelled distribution with a greater than random NN spacing.

Differences in the NN statistics between the paterae ($N = 423$) and patera floor units ($N = 529$ and 581) are explained to the occurrence of multiple volcanic units in association with most patera. This can been seen in the frequency distributions of the paterae and patera floor units (Fig. 6b), where the NN distances between paterae are unimodal with a peak between 150 and 225 km, while the pateae floor units are bimodal, with a sharp primary mode at distances <25 km, and a broad secondary mode between approximately 125 and 200 km. The greater than random NN spacing between generalized paterae can thus be accredited to a disproportional filtering of closely volcanic units that are represented within the primary mode of the patera floor unit distribution.

This example highlights that the spatial organization of patera floor units and generalized paterae differ, and that there is value in considering paterae floor units separately from generalized volcanic systems. Nonetheless, we caution that the distribution was created by dissolving the boundaries between patera floor unit that are confined within topographic depressions, and thus it may exclude both overlapping volcanic systems and volcanic systems that lacking a caldera-like depression. Consequently, we focus our attention on the better defined patera floor units as an indicator of where volcanic activity has occurred on Io, rather than on generalized patera which provide a crude proxy for the structural extent of volcanic systems.

Next we examine NN statistics for hotspots (N =173) and paterae floor units (N = 529) on regional scales. In all hemispheres, hotspots are consistent with the homogeneous Poisson model (Figs. 5c, 5d), whereas paterae floor units exhibit statistically significant clustering in all hemispheres except the antijovian hemisphere. In the antijovian hemisphere, patera floor units exhibit NN distances with a slight tendency towards clustering, but the departure from randomness is not significant at the 2σ level. Using divisions at ±19.47° latitude, hotspots in the north and south polar regions are randomly distributed within 1σ limits of R and c (Figs. 3e, 3f), whereas near-equatorial hotspots are uniform (i.e., repelled from each other). In contrast, patera floor units in the north and south polar regions are clustered, while near-equatorial paterae are randomly distributed.

In summary, hotspots are globally random, but tend toward uniformity near the equator. In contrast, paterae floor are globally clustered, except at low latitudes, where they appear randomly distributed. However, generalized paterae—defined on the basis of topographic depressions—exhibit uniformity on a global scale. This implies that the tendency toward clustering among paterae floor units on a global scale is driven by multiple volcanic units forming in association with most paterae. The primary mode in patera floor unit NN frequency distribution may therefore reflect the spacing of erupted units within a volcanic system, whereas the secondary mode may indicate the spacing between neighboring volcanic systems.

5.2 Distance-based clustering

Random NN distributions imply independent pair-wise formation, but randomly-spaced pairs of points may also be organized into larger groups or clusters consisting of more than two members. Distance-based clustering of volcanic centers using two cluster centers (i.e., k = 2) identifies optimal hotspot concentrations at 17.8ºS, 317.6ºW and 12.7ºN, 136.6ºW (Fig. 7a), whereas patera floor units (N = 529) have optimal cluster centers located at 15.6ºS, 320.5ºW and 1.1ºN, 149.5ºW (Fig. 7b).

The sensitivity analysis identified a large number of potentially significant solutions (see Supplementary Material), but these near-optimal clusters concentrate within a small number of families located close to the global optima (Fig. 8). To characterize the uncertainty in cluster locations, we calculated the maximum mean cluster displacement of the potentially significant solutions from the global optimum. This uncertainty equals 120.6 km for hotspots $k = 2$ (Fig. 8a), and <0.1 km for paterae $k = 2$ (Fig. 8b). The fact that the near-optimal hotspot cluster centers concentrate with closely spaced families, rather than forming a degenerate set of solutions that are widely-distributed over the globe, supports the assertion that hotspots and paterae are meaningfully clustered over large regions.

For the $k = 6$ hotspot solution, the coordinates of the optimum cluster centers are: 41.6ºN, 302.0ºW; 45.6ºS, 294.5ºW; 9.5ºN, 214.5ºW; 37.0ºS, 146.5ºW; 28.0ºN, 114.6ºW; and 2.3ºS, 22.0ºW (Fig. 7c). For the patera floor units (N = 529) optimum cluster centers for the $k = 6$ solution are located at: 3.0ºN, 333.4ºW; 65.2ºS, 300.9ºW; 22.8ºN, 249.2ºW; 22.2ºS, 176.9ºW; 33.5ºN, 135.2ºW; and 20.0ºS, 77.1ºW (Fig. 7d). Uncertainties in $k = 6$ hotspot and patera solutions are <262 km (Fig. 8c) and <92 km (Fig. 8d), respectively. The $k = 6$ hotspot centers exhibit a pattern similar to the distribution of surface heat flux maxima, but with an eastward offset of 30–60º from the tidal axis. In contrast, the $k = 6$ clustering of paterae shows a pattern of cluster centers alternating between the northern and southern hemispheres (Fig. 7d). South of the antijovian point, one of the patera floor clusters shows excellent agreement with a surface heat flux maximum predicted by asthenospheric-dominated solid body tidal heating models (Fig. 8d), but in general the correspondence between cluster centers and the predicted maxima are poor.

6. Discussion: Implications for tidal heating and magma ascent

6.1. Nearest neighbor analyses

We have analyzed the distribution of hotspots and paterae on Io under the assumption that hotspots represent sites of currently active volcanism, whereas patera floor units provide a longer record of Io's volcanic history spanning approximately the past 1 million years (i.e., Io's timescale of its resurfacing). However, given differences between paterae databases and the potential for observational bias given spatially variable image resolution, we regard the volcano databases as statistically samplings, rather than a definitive inventory, and so to mitigate potential sample biases, we limit our NN analyses only to broad regions of Io.

On a global scale, hotspot locations are consistent with a homogeneous Poisson model, which implies that NN hotspot pairs generally form independently of one another. The same random relationship is observed among hotspots in all hemispheres. However, a different pattern emerges when hotspots in the near-equatorial regions are compared to those in near-polar regions. Hotspots in the near-polar regions of Io are randomly distributed, whereas near-equatorial hotspots exhibit a statistically significant departure from randomness (beyond 2σ) that tends toward spatial uniformity (i.e., repelling). Randomly located hotspots near the poles imply the independent formation of volcanic systems at higher latitudes, which may imply a general absence of resource competition relative to the more widely-spaced hotspots near the equator. Repelling among near-equatorial hotspots implies that pair-wise interactions cause these hotspots to form at distances that are larger than would be predicted by the homogeneous Poisson model.

In general, this pattern of spatial organization can be explained by a process that drives features apart in order to maximize the utilization of resources (Baloga et al., 2007). If Io has global asthenosphere with ≥20% interconnected melt (Khurana et al., 2011), then there may be abundant of magma at depth to drive volcanic processes, but the effects of magma chambers and edifies may focus rising dikes in a capture region around each volcano (Karlstrom et al., 2009). In the densely populated near-equatorial region of Io, the magma capture regions around adjacent volcanoes may lead to competition for rising magma and contribute to larger than random NN spacing between hotspots as small volcanic systems are starved of their magma supply and new volcanic centers are inhibited from forming in close proximity to established ones. However, it is possible that other factors such as crustal heterogeneities, mountain blocks, fault distributions, and tectonic controls may also play a role in determining where magma ascends through the crust.

Paterae show different patterns of spatial distribution. Globally, paterae ($N = 423$)—defined as caldera-like topographic depressions—exhibit significant repelling (beyond 2σ) between NN pairs. This implies that patera can interact with one another to form self-organized system with NNs spacing further apart than a homogeneous Poisson model would predict. In contrast, patera floor units—defined as bright, dark, and undifferentiated albedo units inferred to represent the products of discrete episodes of volcanic activity—exhibit global clustering for both the $N = 529$ and 581 distributions.

Hemispherically and in the near-polar regions, NN patera floor units ($N = 529$) tend toward clustering, whereas near-equatorial paterae are well-described by a homogeneous Poisson (i.e., random) distribution. If paterae form when shallow magma chambers are partially depleted and collapse (Wood, 1984), then the presence of smaller paterae at low latitudes (Radebaugh et al. 2001; Williams et al., 2011a) implies that magma chambers at lower latitudes are smaller in size. Given that asthenospheric heating models (e.g., Tackley et al. 2001) predict that there should be ample heat available for magma generation in the equatorial regions, restrictions on crustal magma chamber sizes may result from competition between adjacent volcanic systems. Just as competition for magma may help to drive active hotspots away from one another, a process of dike lensing (Karlstrom et al., 2009) may favor the formation of a small number of large magma chambers that exert a strong influence on their surroundings, thereby limiting the size of other magma chambers and leading to a large number smaller patera. This would explain the overall log-normal distribution of paterae floor areas, which have a geometric mean of 1055 km^2 (+2595 km^2 and -657 km^2 at 1σ). However, even though new volcanic centers would be most likely form at a maximal distance from other active volcanoes, repeated eruption cycles could overprint the distribution of paterae floor units and randomize them through time. In contrast to the randomly spaced near-equatorial patera floor units, patera floor units in the near-polar region appear clustered. This could be explained by paterae concentrating in the vicinity of longer-lived hotspots that are fed from greater depth. This is consistent with models for a thicker lithosphere in the polar region (McEwen et al., 2000a), which relative to the near-equatorial region would lead to larger, and perhaps more stable magmatic upwellings at high latitudes (Radebaugh et al., 2001).

6.2. Frequency distributions

When considering local variations in volcano distributions on Io, it is important to account for spatial variations in image resolution (Fig. 1b). Fortunately, image coverage is generally robust between ±60° latitude (Fig. 3b) and in this region the latitudinal population density of hotspots (Fig. 3a) is consistent with a uniform frequency distribution within 1σ confidence limits (based on χ^2 tests), whereas in the same region paternal floor units (*N* = 529) have a higher population density near the equator. Note that uniformity in population density is not the same as uniformity between the NNs. The former refers to consistency in the number of volcanoes per unit area in different regions, whereas uniformity in the later sense refers to a greater than random pair-rise distance relationship between volcanoes. The uniformity of the hotspot frequency distribution may extend to higher latitudes, but given resolution limitations in the extreme polar regions, deviations from randomness are not statistically significant. The uniformity of hotspot population densities between ±60° latitude suggests that the amplitude of surface heat flux variation in this region is small. This agrees best with mixed tidal heating models that feature a significant deep-mantle component (Figs. 2c, 2d) and/or asthenospheric-dominated models that include surface heat flux averaging effects due to vigorous mantle convection (Fig. 2e).

The longitudinal distribution of population densities exhibits more structure with bimodal peaks in the hotspot distribution at 300–330°W and 120–150°W and in the paterae distribution at 360°–330°W and 150°–180°W (Fig. 3c). The number of volcanic centers (hotspots and paterae) in the region from 30–90°W may be slightly underestimated due to resolution limitations (Fig. 3d), but the generally strong bimodal distributions agrees with asthenospheric tidal heating models that predict a dominant degree-2 pattern of volcanic activity in the near-equatorial region. Nonetheless, the population densities of volcanic centers exhibit a 30–60° eastward offset from the tidal axis, which is not explained by such models.

Correlation of the NN hotspot mode with the secondary NN mode for paterae (Fig. 4c) can be explained if multiple patera floor units tend to form in the vicinity of each hotspot, with isolated patera units being separated by the typical distance between NN hotspots. The primary mode among NN patera floor units may therefore provide an estimate of the length scale over which magmatic pathways branch within the volcanic systems, whereas the modal NN distance between hotspots may be used to constrain the diameter of the magma capture region surrounding major volcanic systems.

6.3. Distance-based clustering

Concentration of hotspots into two near-equatorial clusters supports a dominant role for asthenospheric heating. Within this study, $k = 2$ cluster centers for hotspots and patera floor units are within a few tens of degrees of the maximum concentrations identified among patera structures by Radebaugh et al. (2001), Schenk et al. (2001), Kirchoff et al. (2011), and Veeder et al. (2011). The locations of these antipodal clusters agree with enhanced equatorial heat flux patterns predicted by asthenospheric-dominated models, but they are all offset to the east from the current tidal axis. Nonsynchronous rotation has been invoked as a possible explanation for the eastward offset of paterae from predicted surface heat flux maxima (Radebaugh et al., 2001; Schenk et al., 2001; Kirchoff et al., 2011). However, as an alternative to secondary displacement by faster than synchronous rotation, the eastward offset of volcanic concentrations from the tidal axis may be a consequence of magmatic upwelling in regions that are more favorable for magmatic ascent. For instance, if Io has a global magma ocean (Khurana et al., 2011), then magma could laterally migrate in a subsurface reservoir prior to being erupted. Regions of enhanced volcanism may therefore be related to preferred pathways to the surface rather than directly correlated with sites of maximum heat production. Anisotropies controlling the locations of magma upwelling and enhanced volcanism may include existing fault distributions in the lithosphere and the combination of stresses associated with mantle convection, magma diapirism, magma chambers, shallow intrusions, volcanic conduits, volcanic edifices, mountains, and tidal flexing (McKinnon et al., 2001; Kirchoff and McKinnon, 2009; Kirchoff et al., 2011). However, the existence of global magma ocean (Khurana et al., 2011) also raises the possibility of a fluid tidal response within this silicate melt layer. Tides generated in a layer of interconnected rock melt could generate thermal energy and modify patters of expected surface heat flux in a process analogous to the heating of icy satellites by fluid tidal dissipation and heating within their liquid oceans (e.g., Tyler et al., 2008). The discrepancy between observed concentrations of volcanic centers and the locations of surface heat flux maxima predicted by solid body tidal heating models may therefore reflect a missing component of Io's tidal response, such as the effects of fluid tides generated within a magma ocean. Nonetheless, we cannot rule out the possibility of decoupling of volcanism from sites of maximum heat production by secondary effects such as faster than synchronous rotation and/or state of stress controls of locations of magmatic upwelling.

7. Conclusion

Differences in the spatial organization of neighboring volcanic centers in the near-equatorial and near-polar regions helps to explain the complex distribution of volcanism on Io, which includes components of randomness, clustering, and uniformity. However, the overall concentration of volcanoes at mid- to low-latitudes generally supports asthenospheric-dominated tidal heating, except for an unexplained 30–60° degree eastward offset in concentrations of volcanic centers from predicted surface heat flux maxima. This eastward offset may be explained by: (1) faster than synchronous rotation, (2) state of stress control on the locations of magmatic ascent from a global subsurface reservoir that decouple volcanism from sites of maximum heat production, and/or (3) a missing component of Io's tidal response, such as dissipation and heating by interconnected silicate melt within a global magma ocean.

References

Baloga, S.M., Glaze, L.S., Bruno, B.C., 2009. Nearest-neighbor analysis of small features on Mars: Applications to tumuli and rootless cones. J. Geophys. Res. 112, E03002. doi:10.1029/2005JE002652.

Beggan, C., Hamilton, C.W., 2010. New image processing software for analyzing object size-frequency distribution, geometry, orientation, and spatial distribution. Comp. Geosci. 36, 4, 539–549. doi:10.1016/j.cageo.2009.09.003.

Becker, T., Geissler, P., 2005. Galileo global color mosaics of Io, In Lunar and Planetary Science XXXVI, Abstract #1862, Lunar and Planetary Institute, Houston (CD-ROM).

Běhounková, M., Tobie, G., Choblet, G., Čadek, O., 2010. Coupling mantle convection and tidal dissipation: Applications to Enceladus and Earth-like planets. J. Geophys. Res. 115, E09011. doi:10.1029/2009JE003564.

Carr, M.H., McEwen, A.S., Howard, K.A., Chuang, F.C., Thomas, P., Schuster, P., Oberst, J., Neukum, G., Schubert, G., Galileo Imaging Team, 1998. Mountains and calderas on Io: Possible implications for lithosphere structure and magma generation. Icarus 135, 146–165.

Clark, P.J., Evans, F.C., 1954. Distance to nearest neighbor as a measure of spatial relationships in populations. Ecology 35, 445–453.

Geman, S., Geman, D., 1984. Stochastic relaxation, Gibbs distribution, and the Bayesian restoration of images. IEEE Trans. Pattern Anal. Machine Intell. 6, 721–741.

Hamilton, C.W., Fagents, S.A., Thordarson, T., 2010. Explosive lava–water interactions II: Self-organization processes among volcanic rootless eruption sites in the 1783–1784 Laki lava flow, Iceland. Bull. Volcanol. 72, 4, 469-485. doi:10.1007/s00445-009-0331-5.

Hamilton, C.W., Fagents, S.A., Thordarson, T., 2011. Lava–ground ice interactions in Elysium Planitia, Mars: Geomorphological and geospatial analysis of the Tartarus Colles cone groups. J. Geophys. Res. 116, E03004. doi:10.1029/2010JE003657.

Jaeger, W.L., Turtle, E.P., Keszthelyi, L.P., Radebaugh, J., McEwen, A.S., Pappalardo, R.T., 2003. Orogenic tectonism on Io. J. Geophys. Res. 108, 5093. doi:10.1029/2002JE001946.

{Karlstrom et al., 2009}

{Kesthelyi et al., 2001}

Kesthelyi, L., Jaeger, W., Milazzo, M., Radebaugh, J., Davies, A.G., Mitchell, K.L., 2007. New estimates for Io eruption temperatures: Implications for the interior. Icarus 192, 491–503.

Khurana, K.K., Jia, X., Kivelson, M.G., Nimmo, F., Schubert, G., Russel, C.T., 2011. Evidence of a global magma ocean in Io's interior. Science 332, 1186–1189. doi:10.1126/science.1201425.

Kirchoff, M.R., McKinnon, W.B., 2009. Formation of mountains on Io: variable volcanism and thermal stresses, Icarus 201, 598–614.

Kirchoff, M.R., McKinnon, W.B., Schenk, P.M., 2011. Global distribution of volcanic centers and mountains on Io: Control by asthenospheric heating and implications for mountain formation. Earth Planet. Sci. Lett. 301, 22–30. doi:10.1016/j.epsl.2010.11.018.

Lainey, V., Arlot, J.-E., Karatekin, Ö., Hoolst T. M., 2009. Strong tidal dissipation in Io and Jupiter from astrometric observations. Nature 459, 957–959. doi:10.1038/nature08108.

{Lillesand and Kieffer, 2000}

Lopes-Gautier, R. et al., the Galileo NIMS and SSI Teams. Active volcanism on Io: Global distribution and variations in activity. Icarus 140, 243–264. doi:10.1006/icar.1999.6129.Lopes, R., L. W. Kamp, W.D. Smythe, P. Mouginis-Mark, J. Kargel, J. Radebaugh, E. P.Turtle, J. Perry, D.A. Williams, R.W. Carlson, S. Douté (2004). “Lava Lakes on Io. Observations of Io’s Volcanic Activity from Galileo during the 2001 Fly-bys. *Icarus*, 169/1, pp. 140-174.

Lopes, R.M.C., Spencer, J.R., 2007. Io After Galileo, Springer/Praxis Publishers, Chichester, UK, 342 pp.

McEwen et al., 1998. Active volcanism on Io as seen by Galileo SSI, Icarus, 135, 181–219.

McEwen et al., 2000a. Galileo at Io: Results from high-resolution imaging. Science 288, 1993–1198.

McEwen, A.S., Lopes-Gautier, R., Keszthelyi, L., Keiffer, S.W., 2000b. Extreme volcanism on Jupiter’s moon Io. In: Zimbelmann, J.R., Gregg, T.K.P. (Eds.), Environmental Effects on Volcanic Eruptions: From deep oceans to deep space. Kluwer Academic/Plenum Publishers, New York, USA, 179–205 pp.

McEwen, A.S., Keszthelyi, L.P., Lopes, R., Schenk, P.M., Spencer, J.R., 2004. The lithosphere and surface of Io. In: Bagenal, F., Dowling, T., McKinnon, W. (Eds.), Jupiter: The planet, satellites, and magnetosphere, Cambridge Univ. Press, New York, USA, pp. 307–328.

McKinnon, W.B., Schenk P.M., Dombard, A.J., 2001. Chaos on Io: A model for formation of mountain blocks by crustal heating, melting, and tilting, Geology 29, 103–106.

Moore, W.B., 2001. The thermal state of Io. Icarus 154, 548–550.

Moore, W.B., Schubert, G., Anderson, J.D., Spencer, J.R., 2007. The interior of Io. In: Io After Galileo, Lopes, R. M. C., Spencer J. R. (Eds.), Praxis, Chichester, UK, pp. 89–108.

O'Reilly, T.C., Davies, G.F., 1981. Magma transport of heat on Io: a mechanism allowing a thick lithosphere. Geophys. Res. Lett. 8, 313–316.

Peale, S.J., Cassen, P.R., 1978. Contribution of Tidal Dissipation to Lunar Thermal History. Icarus 36, 245-269.

Peale, S.J., Cassen, P.R., Reynolds T., 1979. Melting of Io by tidal dissipation. Science 203, 4383, 892–894.

Radebaugh, J., Keszthelyi, L.P., McEwen, A.S., Turtle, E.P., Jaeger, W., Milazzo, M., 2001. Paterae on Io: a new type of volcanic caldera? J. Geophys. Res. 106, 33005–33020.

Rathbun, J.A., Spencer, J.R., Davies, A.G., Howell, R.R., Wilson, L., 2002. Loki: A periodic volcano. Geophys. Res. Lett. 29, 10, 1443. doi:10.1029/2002GL014747.

Roberts, J. H., Nimmo, F., 2008. Tidal Heating and the long-term stability of a subsurface ocean on Enceladus. Icarus 194, 675-689.

Rose, K., 1990. Deterministic annealing for clustering, compression, classification, regression, and related optimization problems. Proceedings of the IEEE 86, 11, 2210–2239.

Ross, M.N., Schubert, G., Spohn, T., Gaskell, R.W., 1990. Internal structure of Io and the global distribution of its topography. Icarus 85, 309–325.

Ross, M.N., Schubert, G., 1985. Tidally forced viscous heating in a partially molten Io. Icarus 64, 391–400.

Sabadini, R., and Vermeersen, B., 2004. Global Dynamics of the Earth: Applications of Normal Mode Relaxation Theory to Solid-Earth Geophysics. Kluwer Academic Publishers, Dordrecht.

Shannon, C.E., 1948. A mathematical theory of communication, Bell Syst. Tech. J. 27, 379–423, 623–656.

Smith et al., 1979a. The Galilean satellites and Jupiter – Voyager 2 imaging science results. Science 206, 927–950.

Smith et al., 1979b. The Jupiter system through the eyes of Voyager 1. Science 204, 951–972.

Spencer et al., 2007. Io volcanism seen by New Horizons. Science, 318, 240–243, doi:10.1126/science.1147621.

Spohn, T., 1997. Tides on Io. In: Tidal Phenomena, Lecture Notes in Earth Sciences. Wilhelm, H., Zurn, W., Wenzel, H.G. (Eds.), Springer Verlag, Heidelberg, 66, 345–377.

Schubert, G.T., Spohn, T., Reynolds, R.T., 1986. Thermal histories, compositions and internal structures of the moons of the solar system. In: Satellites, Burns, J.A., Matthews, M. S. (Eds.), Univ. of Arizona Press, Tucson, USA, pp. 224–292.

Schenk, P.M., Hargitai, H., Wilson, R., McEwen A., Thomas, P., 2001. The mountains of Io: Global and geological perspectives from Voyager and Galileo, J. Geophys. Res. 106, 33201–33222.

Segatz, M., Spohn T., Ross, M.N., Schubert, G., 1988. Tidal dissipation, surface heat flow, and figure of viscoelastic models of Io. Icarus 75, 187–206.

Spencer, J.R., Rathbun, J.A., Travis, LD., Tamppari, L.K., Barnard, L., Martin, T.Z., McEwen, A.S., 2000. Io's thermal emission from the Galileo Photopalarimeter-Radiometer. Science 288, 1198–1201.

{Tayler et al., 2000}

Tackley, P.J., Schubert, G., Schenk, P., Ratcliff, J.T., Matas, J.-P., 2001. Three-dimensional simulations of mantle convection in Io. Icarus 149, 79–93. doi:10.1006/icar.2000.6536.

Tackley, P.J., 2001. Convection in Io's asthenosphere: Redistribution of nonuniform tidal heating by mean flows. J. Geophys. Res. 106, E12, 32,971–32,981.

Turcotte, D.L., & Schubert, G., 2002. Geodynamics, 2nd Ed., John Wiley & Sons, New York, USA, 456 pp.

{Turle et al., 2004}

Turtle, E.P., Jaeger, W.L., Schenk, P.M., 2007. Ionian mountains and tectonics: Insights into what lies beneath Io's lofty peaks. In: Io After Galileo, Lopes, R. M. C., Spencer J. R. (Eds.), Praxis, Chichester, UK, pp. 109-131.

Tobie, G., Mocquet, A., Sotin C., 2005. Tidal dissipation within large icy satellites: Applications to Europa and Titan. Icarus 177, 534–549. doi:10.1016/j.icarus.2005.04.006.

Veeder. G.J., Davies, A.G., Matson, D.L., Johnson, T.V., 2009. Io: Heat flow from dark volcanic fields. Icarus 204, 239–253. doi:10.1016/j.icarus.2009.06.027.

Veeder, G.J., Davies, A.G., Williams, D.A., Matson, D.L., Johnson, T.V., Radebaugh, J., 2011. Io: Heat flow from dark paterae. Icarus 212, 236–261. doi:10.1016/j.icarus.2010.09.026.

Wood, C. A., 1984. Calderas: A planetary perspective. J. Geophys. Res. 89, 8391–8406.

{Williams et al., 2002}

{Williams et al., 2004}

{Williams et al., 2005}

Williams, D.A., Keszthelyi, L.P., Crown, D.A., Yff, J.A., Jaeger, W.L., Schenk, P.M., Geissler, P.E., Becker, T.L., 2011a. Volcanism on Io: New Insights from global geologic mapping. Icarus 214, 91–112. doi:10.1016/j.icarus.2011.05.007.

Williams, D.A., Keszthelyi, L.P., Crown, D.A., Yff, J.A., Jaeger, W. L., Schenk, P.M., Geissler, P.E., Becker, T.L., 2011b. Geologic map of Io. U.S. Geol. Surv. Spec. Inves. Map, 1:15,000,000, (in press).

Acknowledgments

C.W.H. is supported by an appointment to the NASA Postdoctoral Program at the Goddard Space Flight Center, administered by Oak Ridge Associated Universities through a contract with NASA. Funding for geological mapping comes to D.A.W. from NASA grants NNG05GH43G and NNX08AQ66G. M.B. is supported by the PRODEX program managed by the European Space Agency and the Belgian Federal Science Policy Office. R.M.C.L. carried out her contribution at the Jet Propulsion Laboratory, California Institute of Technology, under contract with NASA. We thank L. Glaze, L. Kestay, L. Miller, A. Rivoldini, B. Bruno, and R. Tyler for constructive discussions, T. Hare and T. Becker for their assistance exploring the resolution of the original *Galileo-Voyager* imagery, and M. Kirchhoff and an anonymous reviewer for their thorough and insightful reviews. This paper is published with the permission of the British Geological Survey (NERC).

Figures

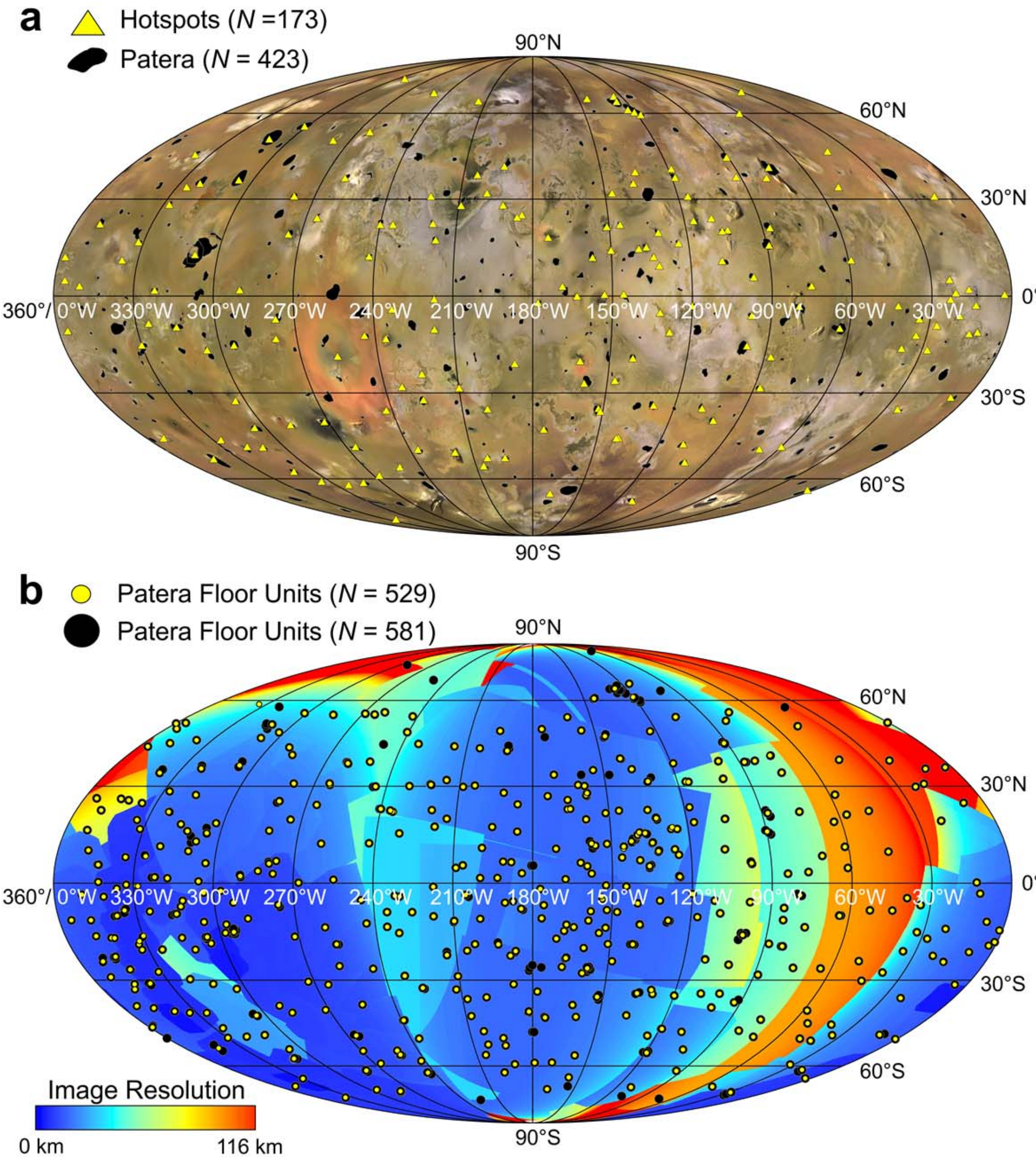

Figure 1. Mollweide projections of the global distribution of volcanoes on Io. a, Hotspots (N = 173) and caldera-like patera (N = 423) overlaid on a *Galileo-Voyager* image mosaics

reprocessed to a spatial resolution of 1 km/pixel (Becker and Geissler, 2005). **b,** Centroids of patera floor units from Williams et al. (2011a) $N = 529$, and Williams et al. (2011b) $N = 581$, overlaid on a map showing the variability of the best imagery used to make the *Galileo-Voyager* basemap. The color ramp has a linear stretch between 0 and 116 km, with a range of resolutions spanning from 0.22 km to 115.54 km. In this study, coordinates are west positive, measured from a prime meridian crossing through the subjovian point of Io.

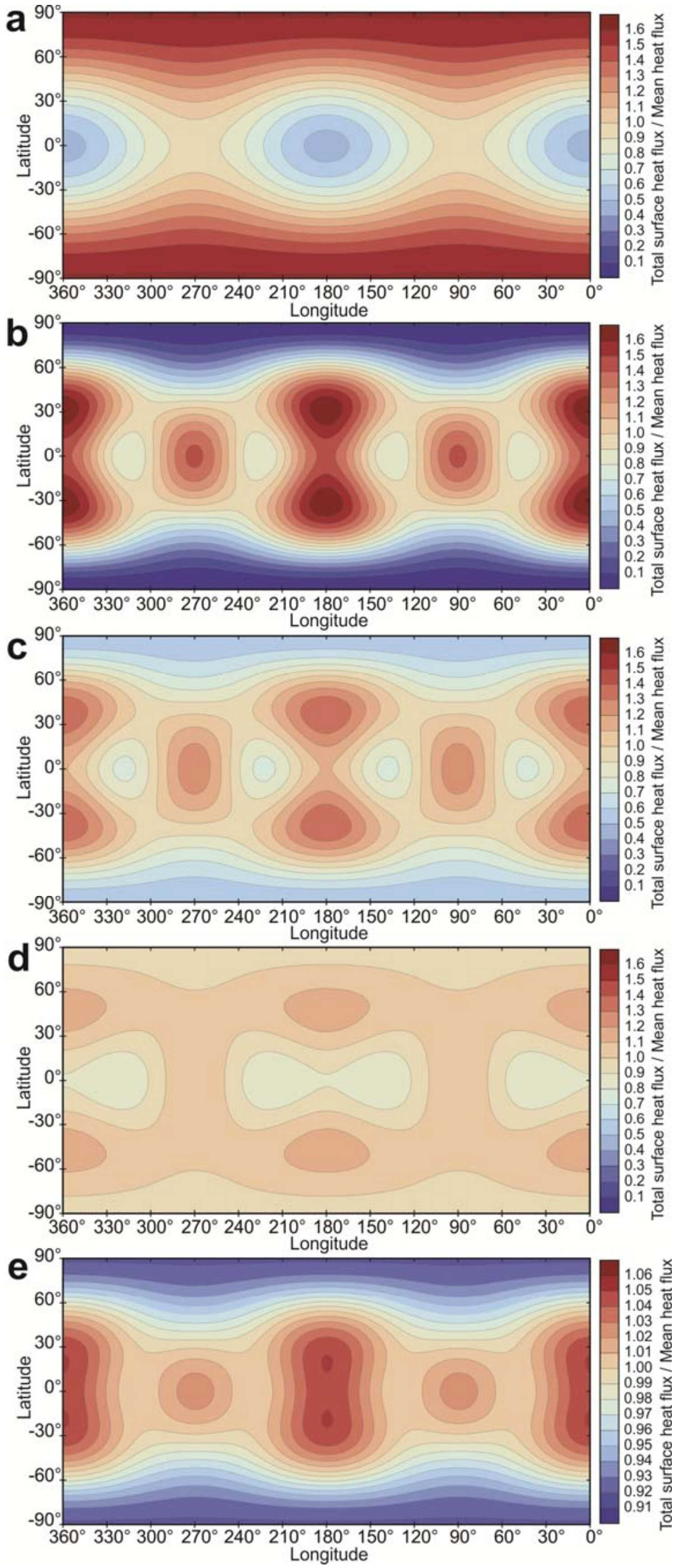
a
b
c
d
e
Latitude
90°
60°
30°
0°
-30°
-60°
-90°
360° 330° 300° 270° 240° 210° 180° 150° 120° 90° 60° 30° 0°
Longitude
Total surface heat flux / Mean heat flux
1.6
1.5
1.4
1.3
1.2
1.1
1.0
0.9
0.8
0.7
0.6
0.5
0.4
0.3
0.2
0.1
1.06
1.05
1.04
1.03
1.02
1.01
1.00
0.99
0.98
0.97
0.96
0.95
0.94
0.93
0.92
0.91

Figure 2. Patterns of surface heat flux due to tidal dissipation for various interior models. **a**, Deep-mantle heating end-member. **b**, Asthenospheric-heating end-member. **c**, Linear combination of end-member models, with the deep-mantle and asthenosphere producing 1/3 and 2/3 of the heat, respectively. **d**, Minimum surface heat flux variation model (<20% variation) generated by a combination of 61% deep-mantle and 39% asthenospheric heating. **e**, Asthenospheric end-member heating pattern averaged by lateral flows due to convection (n.b., change of scale in **e** relative to **a**–**d**). See Methodology for model parameters.

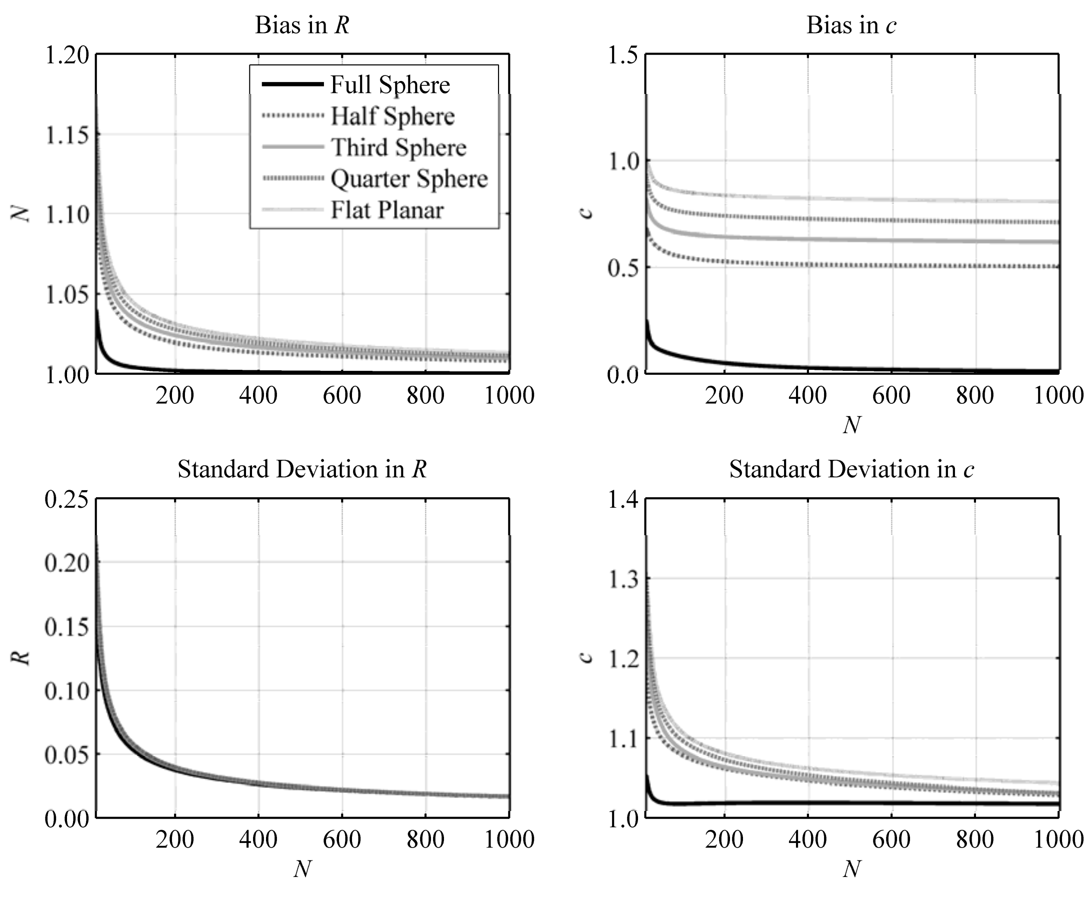

Figure 3. Biases in nearest neighbor (NN) statistics Bias in expected values of R, c, and their standard deviations computed from 4000 Monte-Carlo simulations for a Poisson (i.e., random) distribution for N points on spherical to planar surfaces.

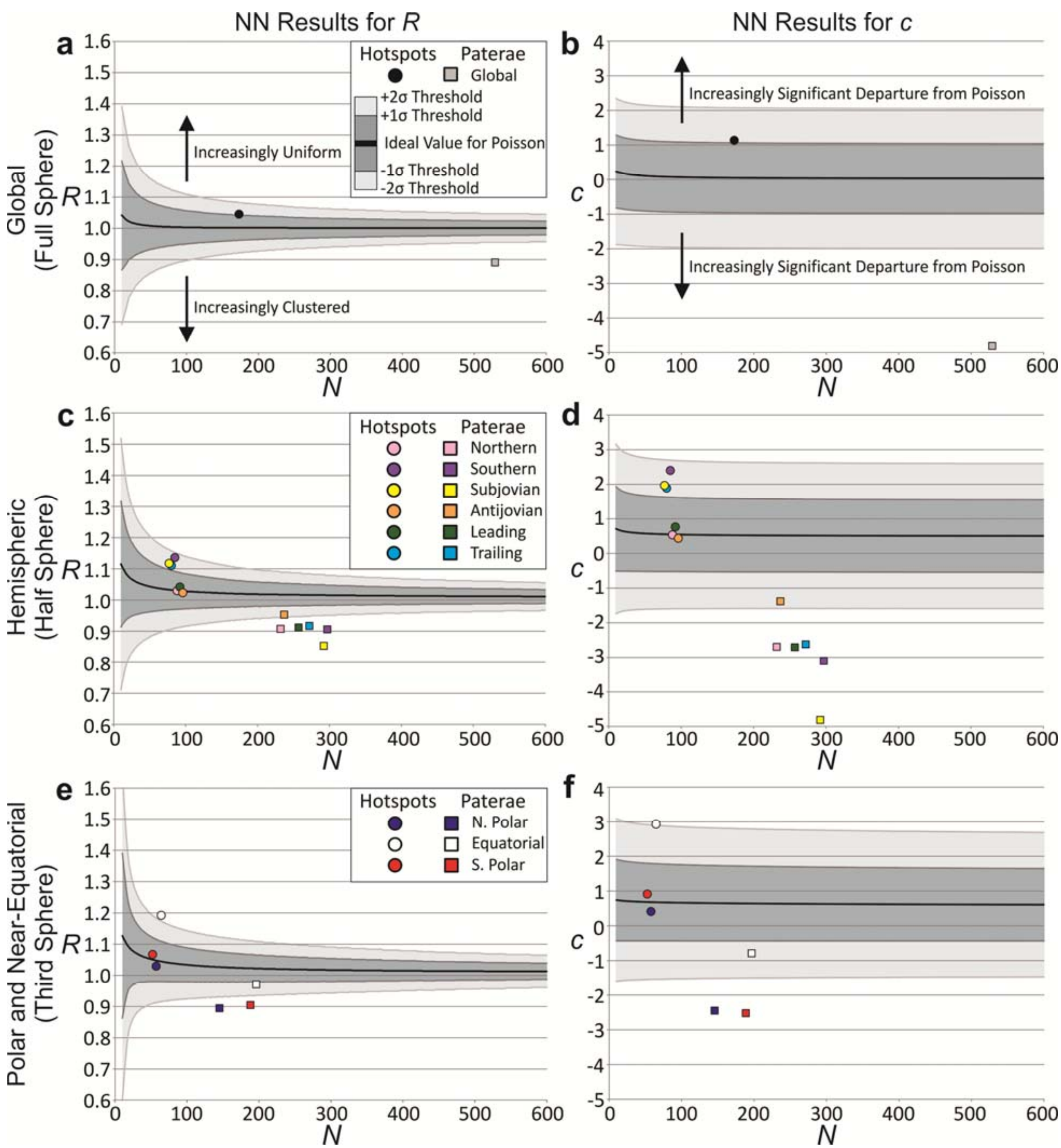

Figure 4. Geodesic nearest neighbor (NN) results for hotspots (*N* = 173) and paterae floor units (*N* = 529). Results for *R* (**a**, **c**, and **e**) and for *c* (**b**, **d**, and **f**). Ideal values for a homogeneous Poisson distribution are represented by black curves, with ±1 and ±2σ confidence limits identified by the upper and lower boundaries of the dark and light grey units, respectively.

To identify statistically significant departures from randomness (i.e., reject the null hypothesis), both R and c must be outside their respective 2σ confidence limits. If R is above the upper 2σ limit, the distribution tends toward uniformity with NN pairs being repelled from one another, whereas if R is below the lower 2σ limit, the distribution tends toward clustering with NN pairs being more closely spaced than predicted by a homogeneous Poisson model. **a** and **b**, Results for the global distribution of volcanic centers. **c** and **d**, Results for each hemisphere. **e** and **f**, Results for the near-equatorial and near-polar regions based ±19.47º latitude divisions.

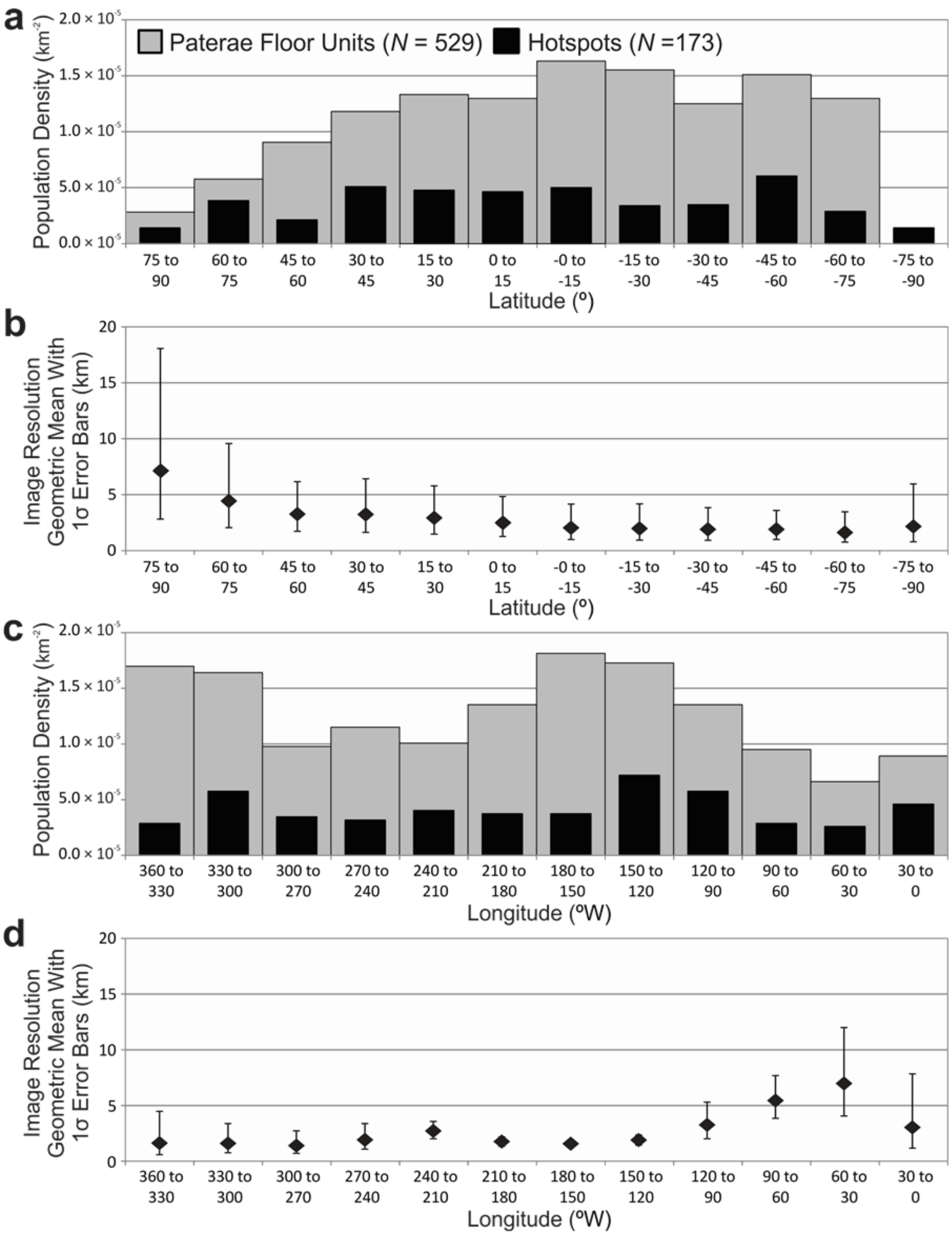

Figure 5. Spatial variability in volcano distributions hotspots (*N* = 173) and paterae (*N* = 529). a, Latitudinal variation. **b,** Longitudinal variation. **c**, Frequency distribution of measured NN distances among the global distributions of hotspots and paterae.

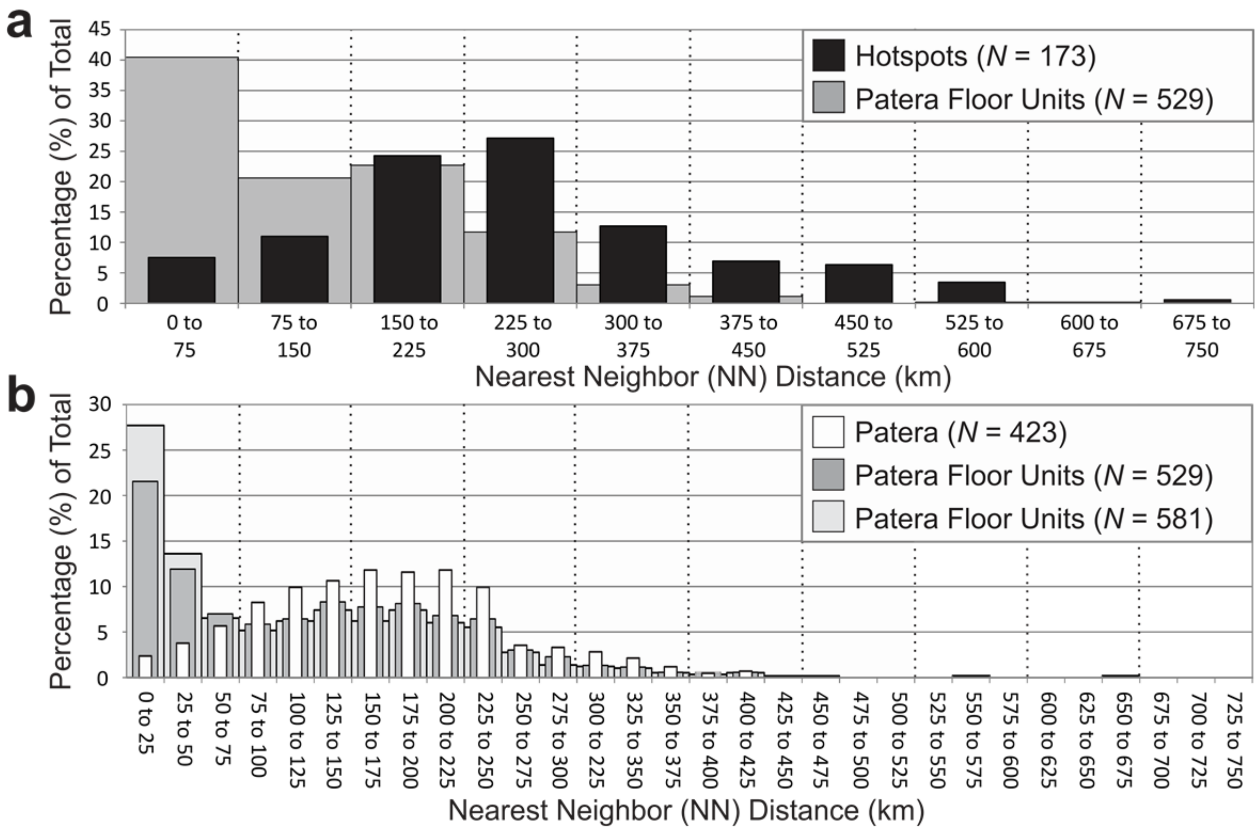

Figure 6. Nearest neighbor (NN) distances between hotspots and paterae on Io. a, Frequency distribution of hotspots ($N = 173$) and patera floor units ($N = 529$) that are the primary focus of this study. **b,** Alternative paterae databases compared to the $N = 529$ distribution. The $N = 581$ distribution is from Williams et al. (2011b) and the generalized patera ($N = 423$) were obtained by calculating the centroids of amalgamated patera floor units that are confined within topographic depressions.

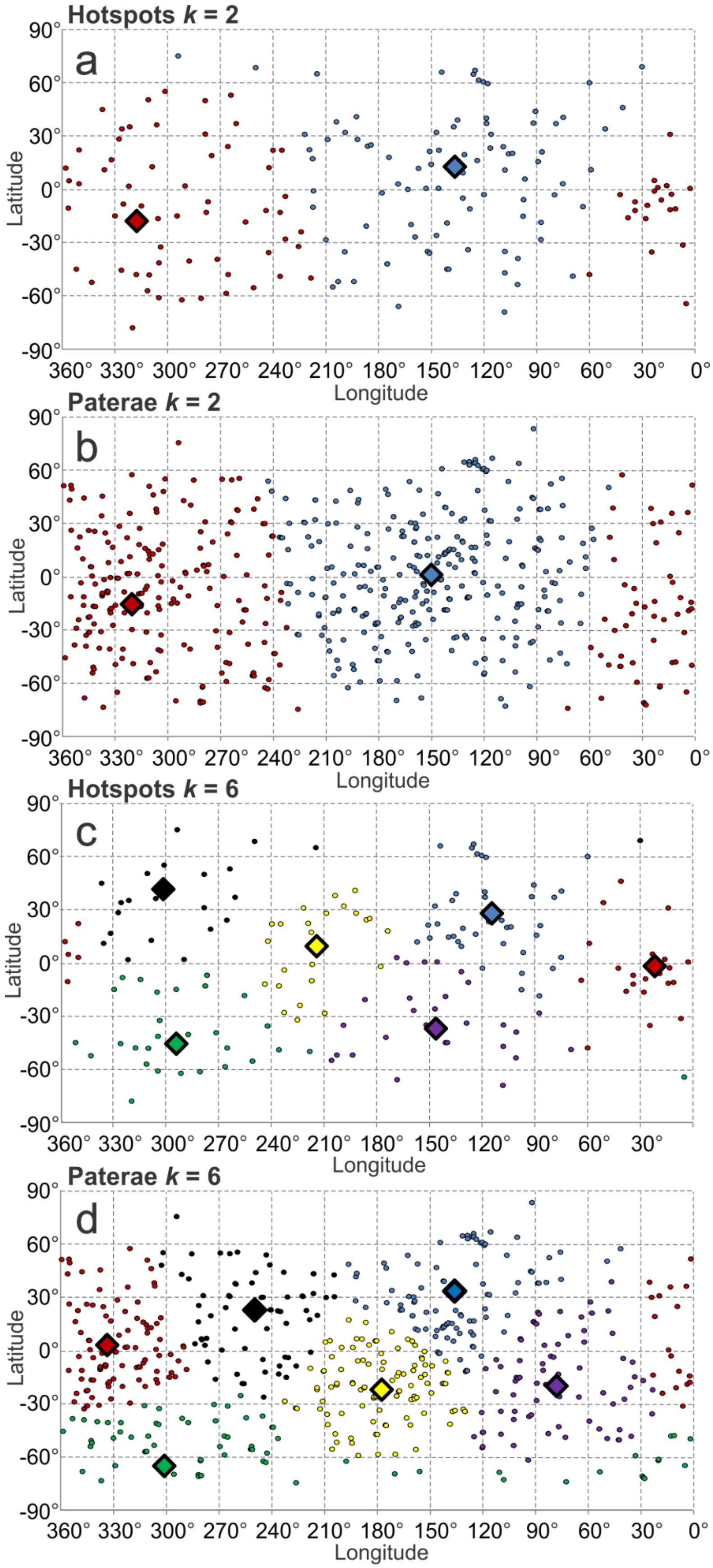

Hotspots k = 2
a
Paterae k = 2
b
Hotspots k = 6
c
Paterae k = 6
d
Latitude
Longitude
90°
60°
30°
0°
-30°
-60°
-90°
360° 330° 300° 270° 240° 210° 180° 150° 120° 90° 60° 30° 0°

Figure 7. Distance-based clustering results. Partitioning with two clusters ($k = 2$) for **a,** hotpots and **b,** paterae. Clustering results with six clusters ($k = 6$) for **c,** hotpots and **d,** paterae. Filled diamonds represent cluster centers and filled circles represent volcanic centers. Shared colors indicate cluster membership. The choice of $k = 2$ and 6 is supported by the results of Kirchoff et al. (2011), which uses spherical harmonic analysis to demonstrate that on a global scale the only statistically significant clustering of volcanic centers (beyond 2σ) occurs at degrees 2 and 6.

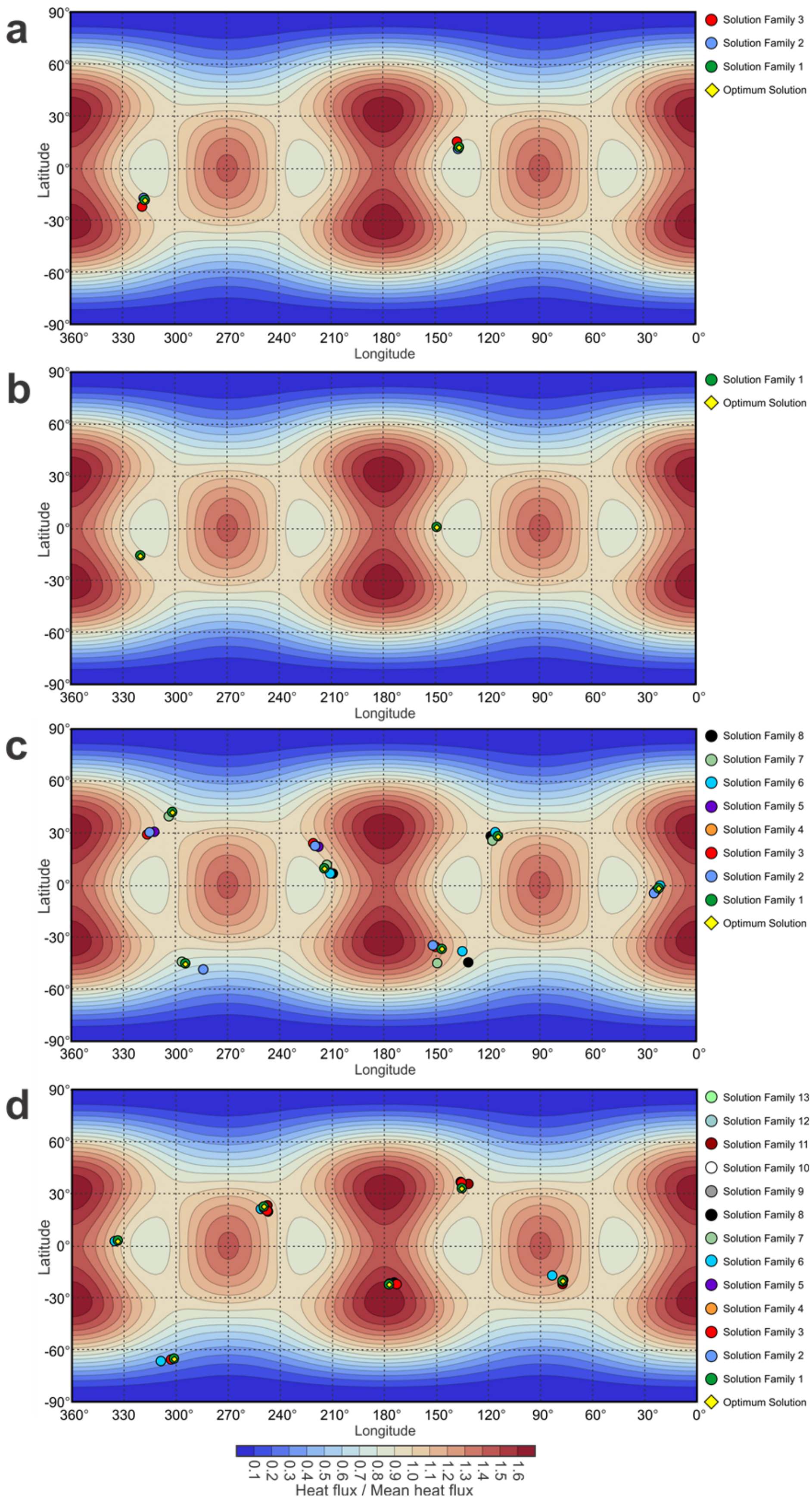
a
b
c
d
Latitude
Longitude
Solution Family 13
Solution Family 12
Solution Family 11
Solution Family 10
Solution Family 9
Solution Family 8
Solution Family 7
Solution Family 6
Solution Family 5
Solution Family 4
Solution Family 3
Solution Family 2
Solution Family 1
Optimum Solution
Heat flux / Mean heat flux

793

Figure 8. Sensitivity analysis of clustering results. Near-optimum cluster center locations for **a**, hotspots (N = 173, k = 2); **b**, patera floor units (N = 529, k = 2); **c**, hotspots (N = 173, k = 6); and **d**, patera floor units (N = 529, k = 6), where k refers to the number of clusters in the analysis. Relative to the optimum solutions (yellow diamonds), the maximum mean cluster offsets among the near-optimal solutions (filled circles) are: <121 km for hotspots k = 2, <1 km for paterae k = 2, 262 km for hotspots k = 6, and 92 km for paterae k = 6. Cluster centers are overplotted on the surface heat flux distribution predicted by the asthenospheric solid body tidal heating end-member (Fig. 2b).